Borràs-Ferrís, J.; Sánchez Tovar, R.; Blasco-Tamarit, E.; Fernández Domene, RM.; Garcia-Anton, J. (2016). Effect of Reynolds number and lithium cation insertion on titanium anodization. Electrochimica Acta. 196:24-32. doi:10.1016/j.electacta.2016.02.160.

Effect of Reynolds number and lithium cation insertion on titanium anodization

J. Borràs-Ferrís[a], R. Sánchez-Tovar[a], E. Blasco-Tamarit[a], R.M. Fernández-Domene[a], J. García-Antón[a]*

[a]*Ingeniería Electroquímica y Corrosión (IEC). Departamento de Ingeniería Química y Nuclear. ETSI Industriales. Universitat Politècnica de València. Camino de Vera s/n, 46022 Valencia, Spain.*

Tel. 34-96-387 76 32, Fax. 34-96-387 76 39, e-mail: jgarciaa@iqn.upv.es

Abstract

This work studies the influence of using hydrodynamic conditions (Reynolds number, Re = 0 to Re = 600) during Ti anodization and Li^+ intercalation on anatase TiO_2 nanotubes. The synthesized photocatalysts were characterized by using Field Emission Scanning Electron Microscope (FE-SEM), Raman Confocal Laser Microscopy, Electrochemical Impedance Spectroscopy (EIS), Mott-Schottky analysis (M-S), photoelectrochemical hydrogen production and resistance to photocorrosion tests. The obtained results showed that the conductivity of the NTs increases with Li^+ intercalation and Re. The latter is due to the fact that the hydrodynamic conditions eliminate part of the initiation layer formed over the tube-tops, which is related to an increase of the photocurrent in the photoelectrochemical water splitting. Besides, the photogenerated electron-hole pairs are facilitated by Li^+ intercalation. Finally, this work confirms that there is a synergistic effect between Re and Li^+ intercalation.

Keywords: TiO_2 nanotubes; hydrodynamic conditions; water splitting; electrochemical impedance spectroscopy (EIS); Mott-Schottky analysis.

1. Introduction

In recent years, nanotube (NT) arrays based on transition-metal oxides are gaining interest in a wide field of applications, such as in dye-sensitized solar cells [1, 2], photocatalysis [3-7] and biomedicine [8]. Among all transition-metal oxides, TiO_2 is the most extensively studied material due to its unique properties. Especially, in photocatalytic reactions, TiO_2 is used as a photocatalyst due to its high stability and semiconductor abilities capable of generating charge by absorbing energy [9-13]. Besides, its suitable band-edge positions make possible the photoelectrochemical water splitting [14] (using solar energy) into H_2 and O_2 to generate hydrogen, the potential fuel of the future.

In order to achieve a high surface area and consequently, to enhance the photocatalytic activity, TiO_2 is synthesized in the form of nanotube arrays [15]. Nowadays, TiO_2 nanotubes are synthesized by several methods, including sol-gel transcription [16, 17], hydrothermal processes [18, 19] and anodization of titanium in fluoride-based electrolytes [20, 21]. The latter is the most promising because it allows obtaining highly ordered nanotube arrays, and their dimensions (length, diameter, and tube wall) can be precisely controlled [22].

In order to carry out the anodization two types of electrolytes can be used: aqueous-based or organic-based. Organic electrolytes are the most used because these electrolytes result in highly ordered longer tubes [23, 24]. Nevertheless, the nanotubes formed in organic electrolytes show an “initiation layer” over the tube tops, which blocks the nanotube arrays and therefore the solar energy absorption is reduced [22, 25].

Nowadays, several methods are investigated to remove this "initiation layer", such as mild sonication [23] and hydrodynamic conditions applied during anodization with a rotating electrode configuration [22]. The latter has the advantage of removing the "initiation layer" in the same process of anodization and, therefore, other independent processes in order to remove this layer are not needed. Moreover, the use of hydrodynamic conditions can significantly affect on the final TiO_2 nanotube geometry [22, 26, 27]. After anodization, an amorphous structure is obtained which implies the presence of a high number of defects. These defects act as recombination centers and a thermal treatment is required in order to convert the amorphous structure into a crystalline one [28].

On the other hand, the efficiency of TiO_2 nanotubes is limited by its wide intrinsic band gap of ≈ 3.2 eV for TiO_2 in anatase phase [29, 30]. Thus, the usable fraction of the solar spectrum which can be exploited is only 5% [31]. In this way, the process of inserting impurities in the TiO_2 NTs is widely used for the purpose of modulating their electrical properties (doping), thus, the efficiency of TiO_2 NTs might be increased. Recently, several works [28, 32, 33] studied the Li^+ cation insertion into TiO_2 lattice and they obtained a drastic change in electronic properties, such as a highly increase in the conductivity of TiO_2 [32, 33]. However, these studies were made in static electrolyte and the influence of hydrodynamic conditions during the anodization process was not evaluated.

In this work, we investigate the synergistic effect between Reynolds number (Re) and Li^+ cation insertion in the TiO_2 lattice in order to optimize the photoelectrochemical water splitting for hydrogen production. To characterize the nanostructures, different

microscopy techniques have been used: Field Emission Scanning Electron Microscope (FE-SEM) and Raman Confocal Laser Microscopy. Additionally electrochemical techniques: Electrochemical Impedance Spectroscopy (EIS) and Mott-Schottky technique (M-S), as well as photoelectrochemical techniques have been also used.

2. Experimental procedure

Anodization was carried out using Teflon coated titanium rod (8 mm in diameter, 99.3 % purity) as the working electrode, i.e. 0.5 cm^2 were exposed to the electrolyte. On the other hand, a platinum mesh was used as the counter electrode. Prior to anodization, titanium surface was abraded with 220 to 4000 silicon carbide (SiC) papers and degreased by sonication in ethanol for 2 minutes. The samples were then mounted in a rotating electrode to perform the anodization under hydrodynamic conditions using a voltage source. Different Reynolds numbers were used: 0, 200, 400 and 600, which correspond to 0, 1728, 3456 and 5185 rpm. Anodization was performed in ethylene glycol, 1M H_2O and 0.05M NH_4F electrolytes at 55 V during 30 minutes. Current density during anodization was measured versus time. After each test, the titanium rod was sliced to characterize the morphology of the obtained nanostructures by using Field Emission Scanning Electron Microscopy (FE-SEM). In order to transform amorphous TiO_2 to an anatase phase structure, the anodized samples were annealed at 450 ºC for 1 hour. The crystalline microstructure of TiO_2 was examined by means of a Raman Confocal Laser microscopy. For these measurements, a 632 nm neon laser with 420 μW was used.

In order to add Li^+ to the obtained nanostructures (doped-nanostructures), samples were immersed in an 1M $LiClO_4$ solution, applying -1.5 $V_{Ag/AgCl}$ during 3 seconds. In this way, Ti^{+4} was reduced to Ti^{+3} and, at the same time, Li^+ was intercalated into the TiO_2 lattice. In order to perform the Li^+ intercalation, a three electrode electrochemical cell was used. The TiO_2 NTs after annealing served as the working electrode, while a Ag/AgCl (3 M KCl) electrode was the reference electrode, and a platinum tip was the counter electrode.

For the electrochemical and photoelectrochemical water splitting tests, an electrochemical cell with the same electrodes and electrode configuration than the used for doping the samples, was employed. The area of the TiO_2 nanostructures (working electrode) exposed to the test solution was 0.13 cm^2. The electrochemical measurements were conducted in a 0.1 M Na_2SO_4 solution using an Autolab PGSTAT302N potentiostat under dark conditions (without irradiation). EIS experiments were conducted at the open circuit potential (OCP) over a frequency range from 100 kHz to 10 mHz with a 10 mV (peak to peak) signal amplitude. Mott–Schottky plots were subsequently obtained by sweeping the potential from the OCP in the negative direction at 10 mV s^{-1} with an amplitude signal of 10 mV at a frequency value of 10 kHz.

The photoelectrochemical experiments were carried out under simulated sunlight condition AM 1.5 (100 mW cm^2) in a 1M KOH solution. Photocurrent vs. voltage characteristics were recorded by scanning the potential from −0.8 $V_{Ag/AgCl}$ to +0.55 $V_{Ag/AgCl}$ with a scan rate of 2 mV s^{-1}. Photocurrent transients as a function of the applied potential were recorded by chopped light irradiation (60 s in the dark and 20 s in

the light). Samples were left at +0.55 $V_{Ag/AgCl}$ in the light for one hour, in order to evaluate their stability against photocorrosion.

3. Results and discussion

3.1. Current density transients during anodization

The growth of the TiO_2 nanotubes was monitored by recording the current density during anodization. **Figure 1** shows that all the samples present three stages. Firstly, in stage I, current density decreases because a compact oxide layer (TiO_2) is formed on titanium [25, 34]. Then, in the second stage (stage II), current density increases due to the fact that fluoride ions present in the electrolyte attack the formed TiO_2 layer, which results in water-soluble $[TiF_6]^{2-}$ species. Thus, the current density increases as the reactive area also increases [25, 35]. Finally, in the third stage (stage III), current density remains almost constant due to the formation and growth of regular nanotubes [25, 26].

The slope corresponding to stage II is different depending on the Reynolds number. **Figure 1** shows that the curves of anodization under hydrodynamic conditions show a higher positive slope in stage II compared to the one obtained at Re = 0. This confirms that diffusion process is favoured due to hydrodynamic conditions. Moreover, since the slope corresponding to stage II increases until Re 400 and it remains almost constant for Re 600, it can be said that hydrodynamic conditions favour the fluoride ions diffusion until Re 400 (the highest increase being obtained between Re 0 and Re 200).

3.2. Field Emission Scanning Electron Microscopy (FE-SEM)

Figures 2, 3 and 4 show the morphology of the samples obtained by electrochemical anodization of TiO_2 under static and hydrodynamic conditions by using a FE-SEM microscope. A porous TiO_2 layer can be observed over the nanotubes, i.e. an initiation layer (**Figures 2a and 2b**). This initiation layer blocks the nanotubes preventing part of the solar radiation from being absorbed at the photoelectrode. **Figure 2b** clearly shows the top of the tubes in delimited areas since parts of the initiation layer was removed. Besides, hydrodynamic conditions applied during anodization mainly affect on three parameters related to the morphology of the nanostructures: the length of the nanotubes, the initiation layer and the thickness of the nanotubes. **Figure 2c** shows that self-organized TiO_2 nanotubes were formed. On the other hand, variations on the morphology after Li^+ intercalation were not observed (not shown in **Figure 2**).

Figure 2d shows the influence of Reynolds number on the length of the nanotubes. The length is higher as the Reynolds number increases. This effect involves an increase of the surface area available for the photocatalytic reactions.

Figure 3 shows the top view of the nanostructures using FE-SEM. It is important to point out that in **Figure 3a** (Re=0) there is a continuous initiation layer, however, this layer begins to detach in certain delimitated areas as hydrodynamic conditions increase (**Figure 3b, 3c and 3d,** corresponding to Re from 200 to 600).

On the other hand, **Figure 4** shows that in those areas where the initiation layer is still attached, an increase in the average diameter of the porous presented in the initiation layer is observed when hydrodynamic conditions are applied in relation to static

conditions (**Figure 4a, 4b and 4c**). Therefore, the entrances of the real tubes become more accessible. Finally, **Figure 4d** shows a decrease of the thickness of TiO_2 nanotubes as hydrodynamic conditions increase, which might reduce the electron-hole recombination process.

3.3. Raman Confocal Laser Microscopy

Evaluation of the crystallinity of the as-prepared and annealed (doped and undoped) TiO_2 nanotubes was carried out by means of Raman Confocal Laser Microscopy. **Figure 5** shows, as an example, the Raman Spectra of the as prepared, undoped and doped nanotubes anodized at Re 600, since no differences were found in the Raman Spectra regardless of the Re used during anodization.

The crystallinity of the TiO_2 nanotubes is evaluated according to the peaks presented in the Raman spectra. Anatase phase shows four peaks in the spectra at roughly 141.7, 396.2, 515.1 and 639.3 cm^{-1} [36-38]. In **Figure 5** it can be observed that the as-prepared TiO_2 nanotubes are characterized by a spectra without peaks, which is in agreement with an amorphous phase. However, annealed (doped and undoped) TiO_2 nanotubes present four characteristics peaks, which correspond to the peaks of the anatase phase. This confirms that annealing at 450 ºC for 1 hour, generates TiO_2 nanotubes with anatase phase. Moreover, the peaks obtained for the annealed, both undoped and doped NTs, are almost the same. Therefore, it can be concluded that there are no significant variations on the crystalline structure after Li^+ intercalation.

3.4. EIS measurements

EIS measurements were performed at open circuit potential (OCP) in order to study the changes caused by the hydrodynamic conditions applied during anodization and the Li^+ cation intercalation. **Figure 6** shows the Nyquist (**Figure 6a**), Bode-phase (**Figure 6b**) and Bode-modulus (**Figure 6c**) plots.

From **Figure 6a**, it is possible to discern that undoped TiO_2 NTs have higher impedance values than the doped TiO_2 NTs. Besides, among the undoped samples, TiO_2 NTs synthesized at Re 0 possess the highest impedance. Bode-phase plots, (**Figure 6b)**, show two unfinished semicircles for the samples anodized at Re 0, Re 200 and Re 400 without Li^+ intercalation, which correspond to the presence of two time constants. However, for the nanotubes synthesized at Re 600 without Li^+ and for all the doped samples, the Bode-phase plots show only one semicircle due to the superposition of the two time constants. The two time constants can be attributed to the formation of the nanotubular layer on top of the compact TiO_2 layer [39, 40]. On the other hand, Bode-modulus plots in **Figure 6c** show a decrease of impedance modulus as hydrodynamic conditions increase at low and intermediate frequencies. Moreover, Li^+ insertion also involves a decrease in the impedance modulus for the same frequency range. Additionally, the impedance at high frequencies in Bode plots corresponds to the resistance of the electrolyte which possesses similar values regardless the Reynolds number and the doping conditions.

EIS experimental data were fitted to an electrical equivalent circuit. The electrical equivalent circuit proposed is shown in **Figure 6d** and it is formed by a resistive

element (R_s), corresponding to the electrolyte resistance, and two groups of resistances and constant phase elements (R-CPE), corresponding to the nanotubular layer (R_1-CPE_1) and the compact TiO_2 layer (R_2-CPE_2) [15, 40]. This electrical equivalent circuit has been already used by other authors. Constant phase elements (CPEs) have been used instead of pure capacitors to account for frequency dispersion and non-ideality. Then, CPEs have been converted into pure capacitances (C) by using the following equation [41, 42]:

$$C = \frac{(Q \cdot R)^{1/\alpha}}{R} \quad \textbf{(1)}$$

where Q is the impedance of the CPE and R corresponds to R_2 when **eq 1** is used to calculate C_2. However, in order to determine C_1, R is calculated according to **eq 2**.

$$\frac{1}{R} = \frac{1}{R_S} + \frac{1}{R_1} \quad \textbf{(2)}$$

Table 1 shows the values of the different parameters which characterize the electrical equivalent circuit. R_s has similar values for all the studied conditions (between 32-42 Ω), since the resistance of the electrolyte remains almost constant. Besides, R_2 is higher than R_1 regardless of the hydrodynamic and doping conditions because the nanotubular layer has higher surface area than the compact TiO_2 layer, i.e., the nanotubes possess a higher conductivity. On the other hand, the CPE constant, α, lies between -1 (pure inductance) and +1 (pure capacitor) [43]. In this work the α values are between 0.5 and 1 which are in agreement with a non-ideal capacitive behavior. **Table 1** shows that α_1 takes values lower than α_2 for all the nanostructures. This confirms that the TiO_2 nanotubes layer is more heterogeneous in comparison to the compact TiO_2 layer, the latter having a behavior similar to an ideal capacitor.

Table 1 also shows that R_1 decreases as Reynolds number increases for the undoped and doped nanotubes, indicating that TiO_2 NTs formed at higher hydrodynamic conditions possess higher conductivities than nanotubes formed at Re = 0. Moreover, C_2 values increase as the Reynolds number increases (regardless the doping conditions), indicating that the thickness of the compact TiO_2 layer decreases, which can be interpreted as a transition from a mostly compact layer to a nanotubular one [40]. Concerning the influence of Li^+ insertion, it can be observed that R_1 decreases significantly when the TiO_2 nanotubes are doped. This fact can be explained by a higher number of controlled defects due to Li^+ intercalation and, therefore, the conductivity is favored.

3.5 Mott-Schottky analysis

The Mott-Schottky analysis is a common tool used for the characterization of the electrochemical capacitance of the semiconductor/electrolyte interface as a function of the applied potential [44]. The Mott-Scottky equation predicts a linear relationship of C_{SC}^{-2} with the applied potential (U), as described by the following equation for an n-type semiconductor [40, 45-47]:

$$\frac{1}{C_{SC}^{2}} = \left(\frac{2}{e \cdot \varepsilon_0 \cdot \varepsilon_r \cdot N_D} \right) \cdot \left(U - U_{FB} - \frac{k \cdot T}{e} \right) \qquad \textbf{(3)}$$

where N_D is the donor density, ε_0 ($8.85 \cdot 10^{-14}$ F/cm) the vacuum permittivity, ε_r the dielectric constant, e the electron charge ($1.60 \cdot 10^{-19}$ C), U_{FB} the flatband potential, k the Boltzmann constant ($1.38 \cdot 10^{-23}$ J/K) and T is the absolute temperature. The dielectric constant varies depending on the Li^+ intercalation, this parameter takes values of 100 for the undoped TiO_2 NTs [48, 49] and a value of 500 is assumed for doped TiO_2

NTs [31]. In fact, Van de Krol claimed that the increase in the dielectric constant may be originated by an increase in the polarizability of the TiO_2 from the intercalated Li^+ cations [45].

Figure 7 shows the Mott-Schottky plots for the undoped and doped TiO_2 nanotubes anodized from Re 0 to Re 600. The results given in **Figure 7** were obtained at the frequency of 10 kHz in dark conditions, since at this high frequency value the capacitances do not depend on the frequency [50, 51]. **Figure 7** shows that the capacitance values are higher for the doped TiO_2 NTs (lower values of C_{SC}^{-2}). In this way, a magnification of the Mott-shottky doped plots have been performed as an inset in **Figure 7,** in order to show the straight lines presented in the doped samples.

Table 2 shows the donor densities determined from the positive slopes of the straight lines in the Mott-Schottky plots using **eq 3**. It can be observed that the donor density notably increases for the doped samples (two orders of magnitude) compared to the undoped ones. The increase in the donor density might be associated with an increase in the number of defects present in the TiO_2 nanotubes due to the Li^+ intercalation. Thus, these defects improve the charge transfer along the nanotubes (this is in agreement with the results obtained by means of EIS, **Table 1**). Concerning to the influence of hydrodynamic conditions, it is possible to observe that the donor density increases, to some extent, as Reynolds number also increases for the undoped samples. This fact indicates that, although the morphology of the TiO_2 nanostructures did not change with Re (i.e, nanotubes were formed in all cases), a higher number of oxygen vacancies and/or Ti^{3+} interstitials were introduced within the TiO_2 NTs structure when anodizing under hydrodynamic conditions. On the other hand, the influence of hydrodynamic

conditions in the donor density for the doped samples is not clear (N_D varies between 1 and 4 x 10^{21} ·cm^{-3}). This might be due to the high influence of the Li^+ insertion that hinders the influence of hydrodynamic conditions.

On the other hand, **Table 2** also shows the U_{FB} values obtained from the intercept of the straight line with the potential axis. The flatband potential is the potential that needs to be applied to the semiconductor to reduce the band bending to zero. Additionally, this electrochemical parameter is related to the potential drop at the depletion space charge layer (U_{SC}) and the applied external potential (U) [15], according to **eq 4**.

$$U_{SC} = U - U_{FB} \quad \textbf{(4)}$$

where U_{SC} is the driving force to separate the photogenerated electron-hole pairs (charge separation). Thus, according to **eq 4**, in order to favor the charge separation, the flatband potential should be high and negative. **Table 2** shows that flatband potential is more negative for the doped TiO_2 NTs than for the undoped ones, which indicates that the charge separation is favored by Li^+ intercalation.

3.6. Photocurrent measurements

Figure 8a shows the photoelectrochemical water splitting tests carried out under simulated sunlight AM 1.5 conditions for the different samples. Regardless of the doping condition, photocurrent densities increase with Reynolds number. This is in agreement with the EIS and M-S measurements (lower R_1 values and higher N_D for higher Re) and FE-SEM images. The high photocurrent densities obtained for the nanostructures anodized at higher Reynolds numbers are related to an increase in the conductivity of the NTs, due to a higher density of defects within their structure, which

favors the current flow [15, 52]. These high photocurrent densities obtained for samples anodized under hydrodynamic conditions are also directly related to an increase in the active area of the nanotubes exposed to the electrolyte with increasing Re. As shown in the FESEM images (**Figures 2, 3 and 4**), hydrodynamic conditions during anodization resulted in longer nanotubes lengths and larger diameters of the nanoporous initiation layer, as well as in a partial removal of the nanoporous initiation layer. It is important to point out that the partial removal of the initiation layer at higher Re contributes to an increase in the photocurrent densities in the water splitting tests. This fact is observed in **Figure 8b,** where the photoresponse of TiO_2 NTs of the same length (~ 6.2 μm), but anodized at different Re, are compared. The only difference between both samples is that the initiation layer of the sample synthesized at Re = 600 was partially removed during the anodization process. Therefore, photocurrent densities increased with increasing Re due to the higher active area of the nanotubes in contact with the electrolyte and due to a slightly increase in the number of defects (**Table 2**). On the other hand, photocurrent densities for Li^+ doped nanotubes are significantly higher than the values obtained for the undoped samples, which can be ascribed to their higher number of defects and flatband potentials (in absolute value) **(Table 2)**. Therefore, there is a better charge transfer and transport in the doped nanotubes.

Additionally, **Figure 8a** shows that the photocurrents under illumination increase with the applied potential. According to **eq 4**, the potential drop at the depletion space charge layer increases when the potential applied is higher, thus, the charge separation is favored. Moreover, the photocurrent density increases with the applied potential until a potential value of -0.3 V for the undoped TiO_2 NTs, whereas the photocurrent increases in the entire range of potential, for the doped TiO_2 NTs. This means that the undoped

TiO_2 NTs are saturated more easily by means of the potential applied in comparison to the doped TiO_2 NTs.

On the other hand, in order to evaluate the stability of the NTs against photocorrosion they were tested under AM 1.5 illumination at 0.55 $V_{Ag/AgCl}$ during 1 hour. **Figure 8c** shows that the formed NTs were stable since the photocurrents generated in the process of water splitting were constant during the tests.

The synergistic effect between hydrodynamic conditions and Li^+ intercalation was studied using the photocurrent densities. **Figure 8d** shows that the combined effect (Re + Doping) is higher than the sum of the individual effects obtained at 0.55 $V_{Ag/AgCl}$. This synergistic effect between the hydrodynamic conditions and the Li^+ doping arises from the higher active areas of the samples anodized at Re > 0 (as shown in **Figures 2, 3** and **4**), thus enhancing the intercalation of Li^+ into the TiO_2 nanotubes structure.

4. Conclusions

This work studied the influence of hydrodynamic conditions applied during anodization, as well as the Li^+ intercalation into TiO_2 lattice in order to increase the photocurrent response in the photoelectrochemical water splitting.

The FE-SEM images show that the influence of hydrodynamic conditions results in an elimination of part of the initiation layer and in an increase of the length of the NTs. These facts involve a higher photocurrent density as Reynolds number increases.

On the other hand, Raman Confocal Laser Microscopy revealed that TiO_2 nanotubes in anatase phase were obtained after annealing at 450ºC during 1 hour. Besides, the Li^+ intercalation does not lead to significant variations on the crystalline structure.

EIS measurements showed that the resistance of the undoped NTs decreases with Re. On the other hand, concerning the Li^+ insertion, the resistance of the doped TiO_2 nanotubes decreases due to a higher number of defects, which was confirmed in the M-S analysis. Besides, M-S analysis showed an increase in the flatband potential (in absolute value) for the doped samples, therefore the photogenerated electron-hole pairs are favored. These results explain the higher photocurrent obtained for the doped samples in the photoelectrochemical water splitting.

The synthesized TiO_2 nanotubes were stable in the test electrolyte under illumination.

A synergistic effect between the hydrodynamic conditions and Li^+ was found to arise from the higher active areas of the samples anodized at Re > 0, thus enhancing the intercalation of Li^+ into the TiO_2 nanotubes structure.

Acknowledgements: Authors would like to express their gratitude for their financial support to the Ministerio of Economía y Competitividad (Project CTQ2013-42494-R).

REFERENCES

[1] B. O´Regan, M. Grätzel. A low-cost, high-efficiency solar cell based on dye-sensitized colloidal TiO_2 films, Nature 353 (1991) 737-740.

[2] P. Roy, D. Kim, K. Lee, E. Spiecker, P. Schmuki. TiO_2 nanotubes and their application in dye-sensitized solar cells, Nanoscale 2 (2010) 45-59.

[3] A. Fujishima, T.N. Rao, D.A. Tryk. Titanium dioxide photocatalysis, J. Photochem. Photobiol. C-Photochem. Rev. 1 (2000) 1-21.

[4] A. Fujishima, X. Zhang, D.A. Tryk. TiO_2 photocatalysis and related surface phenomena, Surf. Sci. Rep. 63 (2008) 515-582.

[5] K. Maeda, K. Domen. Photocatalytic Water Splitting: Recent Progress and Future Challenges, J. Phys. Chem. Lett. 1 (2010) 2655-2661.

[6] J.H. Park, S. Kim, A.J. Bard. Novel carbon-doped TiO2 nanotube arrays with high aspect ratios for efficient solar water splitting, Nano Lett. 6 (2006) 24-28.

[7] J.M. Macak, M. Zlamal, J. Krysa, P. Schmuki. Self-organized TiO2 nanotube layers as highly efficient photocatalysts, Small 3 (2007) 300-304.

[8] J. Park, S. Bauer, K. Von Der Mark, P. Schmuki. Nanosize and vitality: TiO2 nanotube diameter directs cell fate, Nano Lett. 7 (2007) 1686-1691.

[9] M.R. Hoffmann, S.T. Martin, W. Choi, D.W. Bahnemann. Environmental Applications of Semiconductor Photocatalysis, Chem. Rev. 95 (1995) 69–96.

[10] V.F. Stone, R.J. Davis. Synthesis, characterization and photocatalytic activity of titania and niobia mesoporous molecular sieves, Chem. Mater. 10 (1998) 1468–1474.

[11] M. Adachi, Y. Murata, M. Harada, S. Yoshikawa. Formation of Titania Nanotubes with High Photo-Catalytic Activity, Chem. Lett. 8 (2000) 942-943.

[12] T. Sreethawong, Y. Suzuki, S. Yoshikawa. Photocatalytic evolution of hydrogen over nanocrystalline mesoporous titania prepared by surfactant-assisted templating sol-gel process, Catal. Commun. 6 (2005) 119-124.

[13] C.C. Tsai, J.N. Nian, H. Teng. Mesoporous nanotube aggregates obtained from hydrothermally treating TiO_2 with NaOH, Appl. Surf. Sci. 253 (2006) 1898–1902.

[14] I. Paramasivam, H. Jha, N. Liu, P. Schmuki. A Review of Photocatalysis using Self-organized TiO_2 Nanotubes and Other Ordered Oxide Nanostructures, small 8 (2012) 3073-3103.

[15] R. Sánchez-Tovar, R. M. Fernández-Domene, D. M. García-García, J. García-Antón. Enhancement of photoelectrochemical activity for water splitting by controlling hydrodynamic conditions on titanium anodization, J. Power Sources 286 (2015) 224-231.

[16] T. Kasuga, M. Hiramatsu, A. Hoson, T. Sekino and K. Niihara. Formation of Titanium Oxide Nanotube, Langmuir 14 (1998) 3160-3163.

[17] J. H. Jung, H. Kobayashi, K. J. C. Van Bommel, S. Shinkai, T. Shimizu. Creation of novel helical ribbon double-layered nanotube TiO_2 structures using an organogel template, Chem. Mater. 14 (2002) 1445-1447.

[18] D. V. Bavykin, J. M. Friedrich, F. C. Walsh. Protonated titanates and TiO2 nanostructured materials: synthesis, properties, and applications, Adv. Mater. 18 (2006) 2807-2824.

[19] D. V. Bavykin, V. N. Parmon, A. A. Lapkin, F. C. Walsh. The effect of hydrothermal conditions on the mesoporous structure of TiO2 nanotubes, J. Mater. Chem. 14 (2004) 3370-3377.

[20] V. Zwilling, E. Darque-Ceretti, A. Boutry-Forveille, D. David, M. Y. Perrin, M. Aucouturier. Structure and physicochemistry of anodic oxide films on titanium and TA6V alloy, Surf. Interface Anal. 27 (1999) 629-637.

[21] J. M. Macak, H. Tsuchiya, P. Schmuki. High-Aspect-Ratio TiO_2 Nanotubes by Anodization of Titanium, Angew. Chem. Int. Ed. 44 (2005) 2100-2102.

[22] R. Sánchez-Tovar, I. Paramasivam, K. Lee, P. Schmuki. Influence of hydrodynamic conditions on growth and geometry of anodic TiO_2 nanotubes and their use towards optimized DSSCs, J. Mater. Chem. 22 (2012) 12792-12795.

[23] T. T. Isimjan, S. Rohani, A. K. Ray. Photoelectrochemical water splitting for hydrogen generation on highly ordered TiO_2 nanotubes fabricated by using Ti as cathode, Int. J. Hydrogen Energ. 37 (2012) 103-108.

[24] Paulose M, Prakasam HE, Varghese OK, Peng L, Popat KC, Mor GK, et al. TiO2 nanotube arrays of 1000 mm length by anodization of titanium foil: phenol red diffusion, J. Phys. Chem. C 111 (2007) 14992-14997.

[25] P. Roy, S. Berger, P. Schmuki. TiO_2 Nanotubes: Synthesis and Applications, Angew. Chem. Int. Ed. 50 (2011) 2904-2939.

[26] R. Sánchez-Tovar, K. Lee, J. García-Antón, P. Schmuki. Formation of anodic TiO_2 nanotube or nanosponge morphology determined by the electrolyte hydrodynamic conditions, Electrochem. Commun. 26 (2013) 1-4.

[27] R. Sánchez-Tovar, K. Lee, J. García-Antón, P. Schmuki. Photoelectrochemical poperties of anodic TiO_2 nanosponge layers, ECS Electrochem. Lett. 2 (2013) 9-11.

[28] A. Ghicov, P. Schmuki. Self-ordering electrochemistry: a review on growth and functionality of TiO_2 nanotubes and other self-aligned MO_x structures, Chem. Commun. 20 (2009) 2791-2808.

[29] R. Beranek, H.Tsuchiya, T. Sugishima, J.M. Macak, L. Taveira, S. Fujimoto, H. Kisch, P. Schmuki. Enhancement and limits of the photoelectrochemical response from anodic TiO2 nanotubes, Appl. Phys. Lett. 87 (2005) 243114-243114-3.

[30] H. Tsuchiya, J. M. Macak, A. Ghicov, A. S. Räder, L. Taveira, P. Schmuki. Characterization of electronic properties of TiO_2 nanotube films, Corrosion Sci. 49 (2007) 203.

[31] L. k. Tsui, M. Saito, T. Homma, G. Zangari. Trap-state passivation of titania nanotubes by electrochemical doping for enhanced photoelectrochemical performance, J. Mater. Chem. A 3 (2015) 360-367.

[32] R. Hahn, A. Ghicov, H. Tsuchiya, J. M. Macak, A. G. Muñoz, P. Schmuki. Lithium-ion insertion in anodic TiO_2 nanotubes resulting in high electrochromic contrast, Phys. Status Solidi A 204 (2007) 1281-1285.

[33] J. M. Macak, B. G. Gong, M. Hueppe, P. Schmuki. Filling of TiO_2 Nanotubes by Self-Doping and Electrodeposition, Adv. Mater. 19 (2007) 3027-3031.

[34] K. Shankar, G. K. Mor, H. E. Prakasam, S. Yoriya, M. Paulose, O. Varghese, C. A. Grimes. Highly-ordered TiO_2 nanotube arrays up to 220 mm in length: use in water photoelectrolysis and dye-sensitized solar cells, Nanotechnology 18 (2007) 065707 (11pp).

[35] D. Regonini, C. R. Bowen, A. Jaroenworaluck, R. Stevens. A review of growth mechanism, structure and crystallinity of anodized TiO_2 nanotubes, Mater. Sci. Eng. R 74 (2013) 377-406.

[36] Leonardo L. Costa, Alexandre G.S. Prado. TiO2 nanotubes as recyclable catalyst for efficient photocatalytic degradation of indigo carmine dye, J. Photochem. Photobiol. A-Chem. 201 (2009) 45–49.

[37] P.T. Hsiao, K.P. Wang, C.W. Cheng, H.S. Teng. Nanocrystalline Anatase TiO_2 Derived from a Titanate-Directed Route for Dye-Sensitized Solar Cells, J. Photochem. Photobiol. A 188 (2007) 19–24.

[38] L. Qian, Z.L. Du, S.Y. Yang, Z.S. Jin. Raman-study of titania nanotube by soft chemical-process, J. Mol. Struct. 749 (2005) 103–107.

[39] V.A. Alves, R.Q. Reis, I.C.B. Santos, D.G. Souza, T. de F. Gonçalves, M.A. Pereira-da-Silva, A. Rossi, L.A. da Silva. *In situ* impedance spectroscopy study of the electrochemical corrosion of Ti and Ti–6Al–4V in simulated body fluid at 25 °C and 37 °C, Corrosion Sci. 51 (2009) 2473-2482.

[40] D. P. Oyarzún, R. Córdova, O. E. Linarez Pérez, E. Muñoz, R. Henríquez, M. López Teijelo, H. Gómez. Morphological, electrochemical and photoelectrochemical characterization of nanotubular TiO_2 synthetized electrochemically from different electrolytes, J. Solid State Electrochem. 15 (2011) 2265-2275.

[41] G. J. Brug, A. L. G. van den Eeden, M. Sluyters-Rehbach, J. H. Sluyters. The analysis of electrode impedances complicated by the presence of a constant phase element, J. Electroanal. Chem. 176 (1984) 275-295.

[42] B. Hirschorn, M.E. Orazem, B. Tribollet, V. Vivier, I. Frateur, M. Musiani. Determination of effective capacitance and film thickness from constant-phase-element parameters, Electrochim. Acta 55 (2010) 6218-6227.

[43] R.M. Fernández-Domene, R. Sánchez-Tovar, C. Escrivà-Cerdán, R. Leiva-García, J. García-Antón. Study of Passive Films Formed on AISI 316L

Stainless Steel in Non-Polluted and Underwater-Volcano-Polluted Seawater, Corrosion Sci. 70 (2014) 390-401.

[44] A. G. Muñoz. Semiconducting properties of self-organized TiO2 nanotubes, Electrochim. Acta 52 (2007) 4167-4176.

[45] R. van de Krol, A. Goossens, J. Schoonman. Spatial Extent of Lithium Intercalation in Anatase TiO_2, J. Phys. Chem. B 103 (1999) 7151-7159.

[46] Bard, A. J.; Faulkner, L. R. Electrochemical Methods, Wiley: New York (1980).

[47] Morrison, S. R. Electrochemistry of Semiconductor and Oxidized Metal Electrodes, Plenum Press: New York (1980).

[48] L. Aïnouche, L. Hamadou, A. Kadri, N. Benbrahim, D. Bradai. Interfacial Barrier Layer Properties of Three Generations of TiO_2 Nanotube Arrays, Electrochim. Acta 133 (2014) 597-609.

[49] A. Hagfeldt, H. Lindström, S. Södergren, Sten-Eric Lindquist. Photoelectrochemical studies of colloidal TiO_2 films: The effect of oxygen studied by photocurrent transients, J. Electroanal. Chem. 381 (1995) 39-46.

[50] M. Radecka, M. Rekas, A. Trenczek-Zajac, K. Zakrzewska. Importance of the band gap energy and flat band potential for application of modified TiO_2 photoanodes in water photolysis, J. Power Sources 181 (2008) 46-55.

[51] M. Radecka, M.Wierzbicka, S.Komornicki, M. Rekas. Influence of Cr on photoelectrochemical properties of TiO_2 thin films, Phys. B 348 (2004) 160–168.

[52] P. Xiao, D. Liu, B. Batalla Garcia, S. Sepehri, Y. Zhang, G. Cao. Electrochemical and photoelectrical properties of titania nanotube arrays annealed in different gases, Sensor Actuat. B-Chem. 134 (2008) 367-372.

Tables captions

Table 1. Values of the equivalent circuit parameters for the different samples anodized at Re = 0, Re = 200, Re = 400 and Re = 600, without and with Li^+-doping (D).

Table 2. Values of the donor density (N_D) and flatband potential (U_{FB}) for the different samples anodized at Re = 0, Re = 200, Re = 400 and Re = 600, without and with Li^+-doping (D).

Figures captions

Figure 1. Current density transients obtained during the potentiostatic anodization of Ti at 55 V at different Reynolds number (Re = 0, Re = 200, Re = 400 and Re = 600).

Figure 2. (a, b) FE-SEM images of the top-view of the TiO_2 NTs anodized at Re = 600 and the initiation layer; (c) the cross sectional view of the NTs anodized at Re = 600; (d) length of the nanotubes vs. Reynolds number.

Figure 3. FE-SEM images of the initiation layer at (a) Re = 0, (b) Re = 200, (c) Re = 400 and (d) Re = 600.

Figure 4. FE-SEM images of the pores of the initiation layer for the samples anodized at (a) Re = 0 and (b) Re = 200; (c) pore size of the initiation layer vs. Reynolds number; (d) wall thickness of the nanotubes vs. Reynolds number.

Figure 5. Raman confocal laser spectra of the as-prepared and annealed at 450 ºC during 1 h (undoped and doped) TiO_2 NTs anodized at 55 V, during 30 min at Re = 600.

Figure 6. Experimental Nyquist (a), Bode-phase (b) and Bode-modulus (c) plots for the samples anodized at Re = 0, Re = 200, Re = 400 and Re = 600, with and without Li^+-doping; (d) electrical equivalent circuit used to simulate experimental EIS data.

Figure 7. Mott Schottky plots, obtained at a frequency of 10 kHz, of the undoped and doped nanotubes anodized at 55 V, during 30 min at Re = 0, Re = 200, Re = 400 and Re = 600.

Figure 8. (a) Photocurrent transient vs. potential curves of the samples anodized at Re = 0, Re = 200, Re = 400 and Re = 600 with and without Li^+-doping under AM 1.5 illumination; (b) photocurrent densities vs potential registers carried out under AM 1.5 for two TiO_2 nanotubes of the same length (~6.2 microns) anodized in ethylene glycol/water/NH4F electrolytes at Re = 0 and Re = 600; (c) photostability experiments carried out under AM 1.5 illumination at 0.55 $V_{Ag/AgCl}$ of the samples anodized at Re = 0, Re = 200, Re = 400 and Re = 600 with and without Li^+-doping; (c) synergistic effect between the influence of hydrodynamic condition and Li^+ intercalation for different hydrodynamic conditions.

Graphical Abstract (for review)

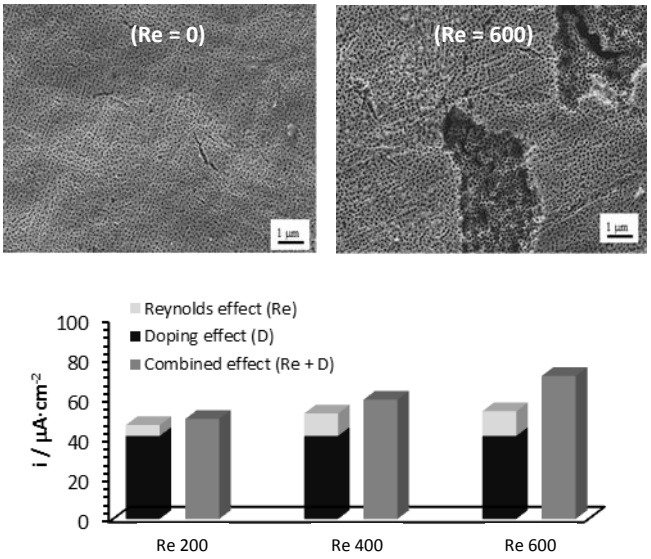

There is a synergistic effect between Reynolds number and Li^+ intercalation on TiO_2 nanotubes for hydrogen production by means of photoelectrochemical water splitting.

Research Highlights

Hydrodynamic conditions during anodization remove part of the initiation layer

Hydrodynamic conditions during anodization led to higher photocurrent densities

The conductivity of the NTs increases with Li^+ intercalation

There is a synergistic effect among the hydrodynamic conditions and Li+ intercalation

Doped nanotubes were stable in the test electrolyte under illumination

Table 1

Re	R_S/Ω cm^2	C_1/μF *cm-2*	α_1	R_1/*kΩ cm2*	C_2/μF cm^{-2}	α_2	R_2/kΩ cm^2	χ^2 (x10^{-3})
0	38 ± 4	106 ± 14	0.68 ± 0.03	5.7 ± 1.8	1690 ± 78	0.98 ± 0.02	78.3 ± 21	5.3
200	39 ± 3	279 ± 11	0.63 ± 0.04	5.1 ± 1.3	1903 ± 84	0.95 ± 0.01	39.4 ± 23	9.6
400	42 ± 5	475 ± 17	0.56 ± 0.08	4.4 ± 1.5	1942 ± 101	0.95 ± 0.03	24.8 ± 12	8.5
600	34 ± 7	132 ± 18	0.74 ± 0.07	2.5 ± 1.0	2399 ± 97	0.97 ± 0.04	38.4 ± 11	8.0
0 - D	32 ± 3	12413 ± 52	0.91 ± 0.03	1.9 ± 0.7	3360 ± 132	0.98 ± 0.02	18.3 ± 8	7.4
200 - D	32 ± 4	4560 ± 97	0.88 ± 0.05	1.7 ± 0.4	3394 ± 112	0.95 ± 0.02	36.2 ± 12	2.3
400 - D	36 ± 5	5865 ± 63	0.87 ± 0.06	1.4 ± 0.5	3900 ± 168	0.95 ± 0.04	31.9 ± 13	3.2
600 - D	27 ± 8	6655 ± 75	0.86 ± 0.04	1.0 ± 0.4	4942 ± 150	0.89 ± 0.03	28.0 ± 9	3.1

Table 2

Re	N_D **(× 10^{19} cm^{-3})**	U_{FB} **/V vs (Ag/AgCl)**
0	1.8 ± 0.3	-0.19 ± 0.05
200	2.1 ± 0.3	-0.10 ± 0.03
400	3.9 ± 0.5	-0.09 ± 0.05
600	3.6 ± 0.4	-0.09 ± 0.02
0 - Doped	390 ± 10	-1.58 ± 0.09
200 - Doped	107 ± 9	-0.70 ± 0.08
400 - Doped	192 ± 12	-1.08 ± 0.03
600 - Doped	278 ± 11	-1.06 ± 0.09

Figure 1

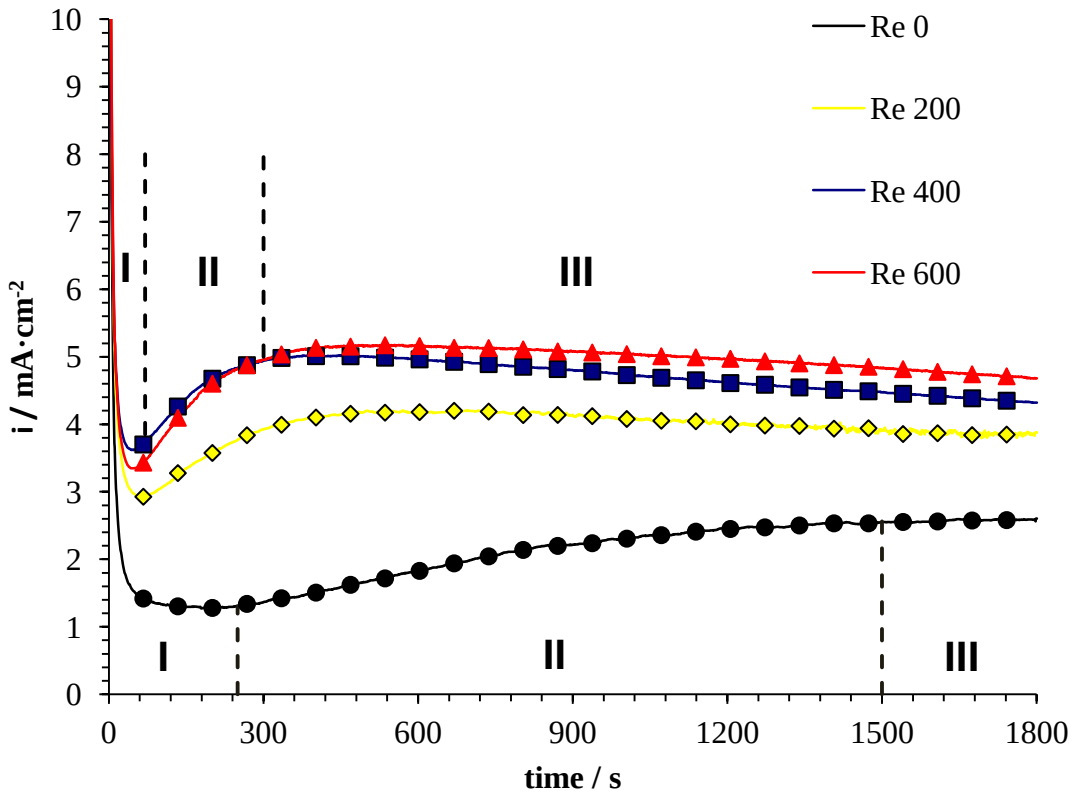
Re 0
Re 200
Re 400
Re 600
i / mA·cm-2
time / s
I
II
III
I
II
III
0
1
2
3
4
5
6
7
8
9
10
0
300
600
900
1200
1500
1800

Figure 2

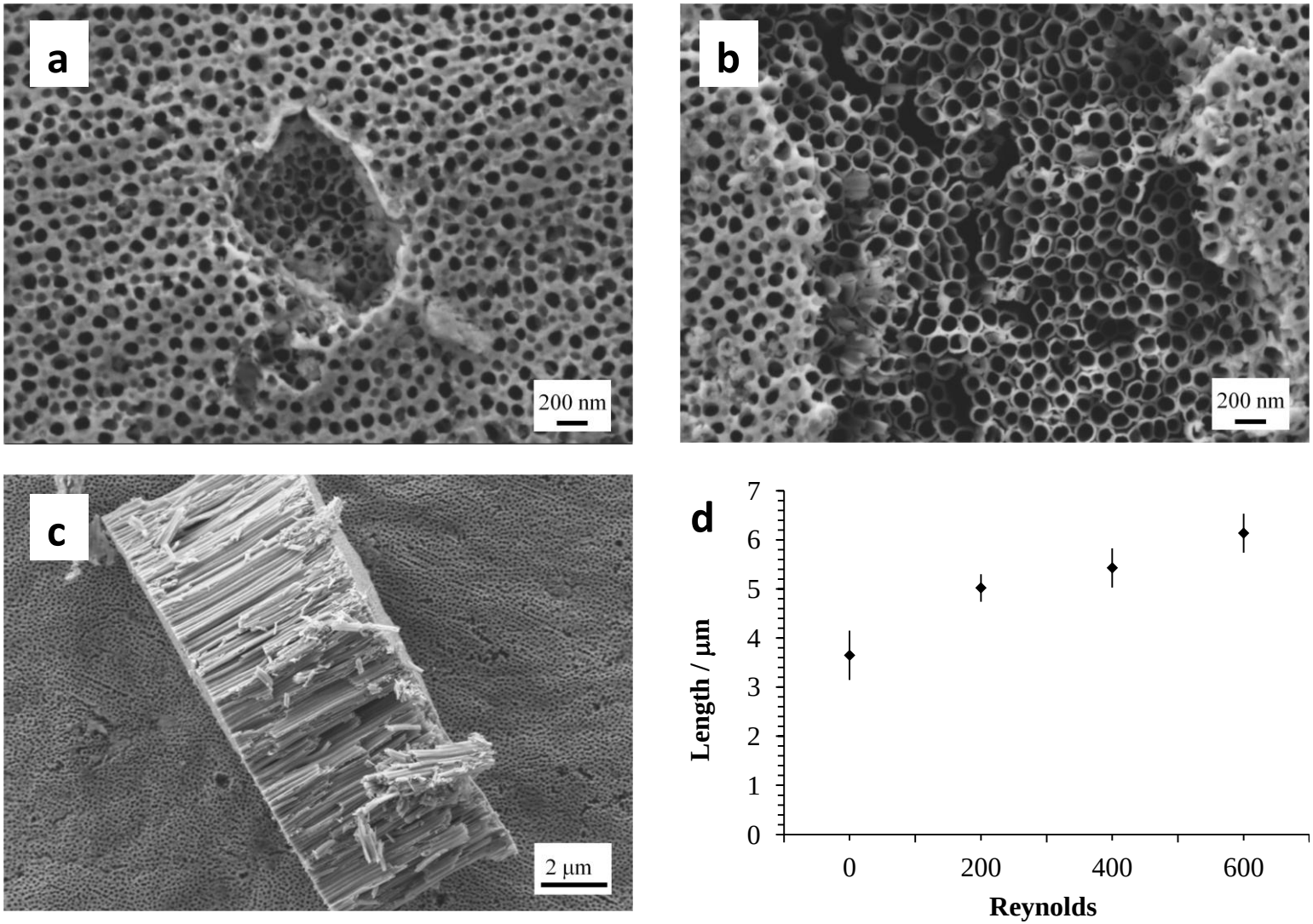
a
200 nm
b
200 nm
c
2 µm
d
Length / µm
0
1
2
3
4
5
6
7
0
200
400
600
Reynolds

Figure 3

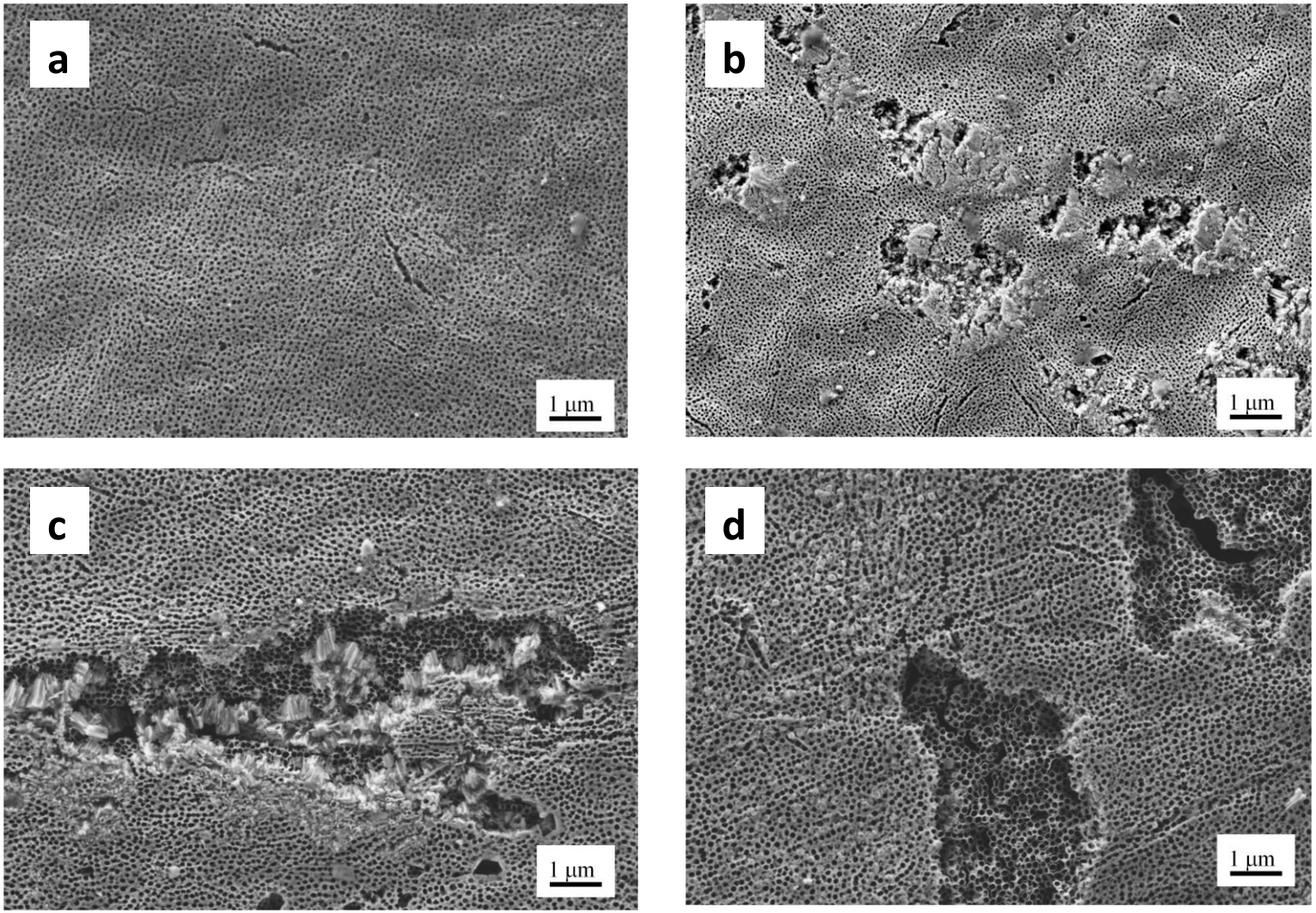

Figure 4

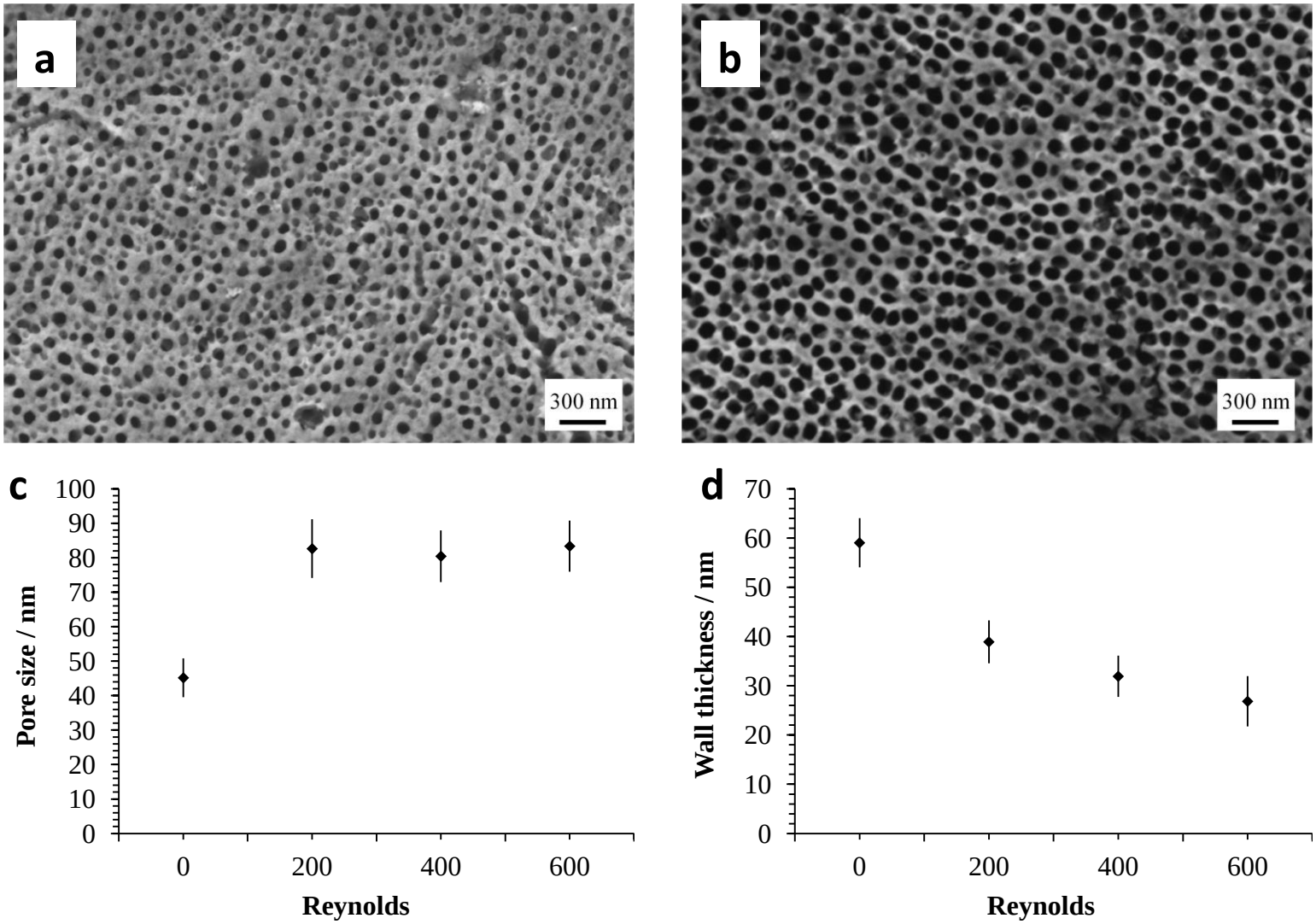
a
300 nm
b
300 nm
c
Pore size / nm
100
90
80
70
60
50
40
30
20
10
0
0
200
400
600
Reynolds
d
Wall thickness / nm
70
60
50
40
30
20
10
0
0
200
400
600
Reynolds

Figure 5

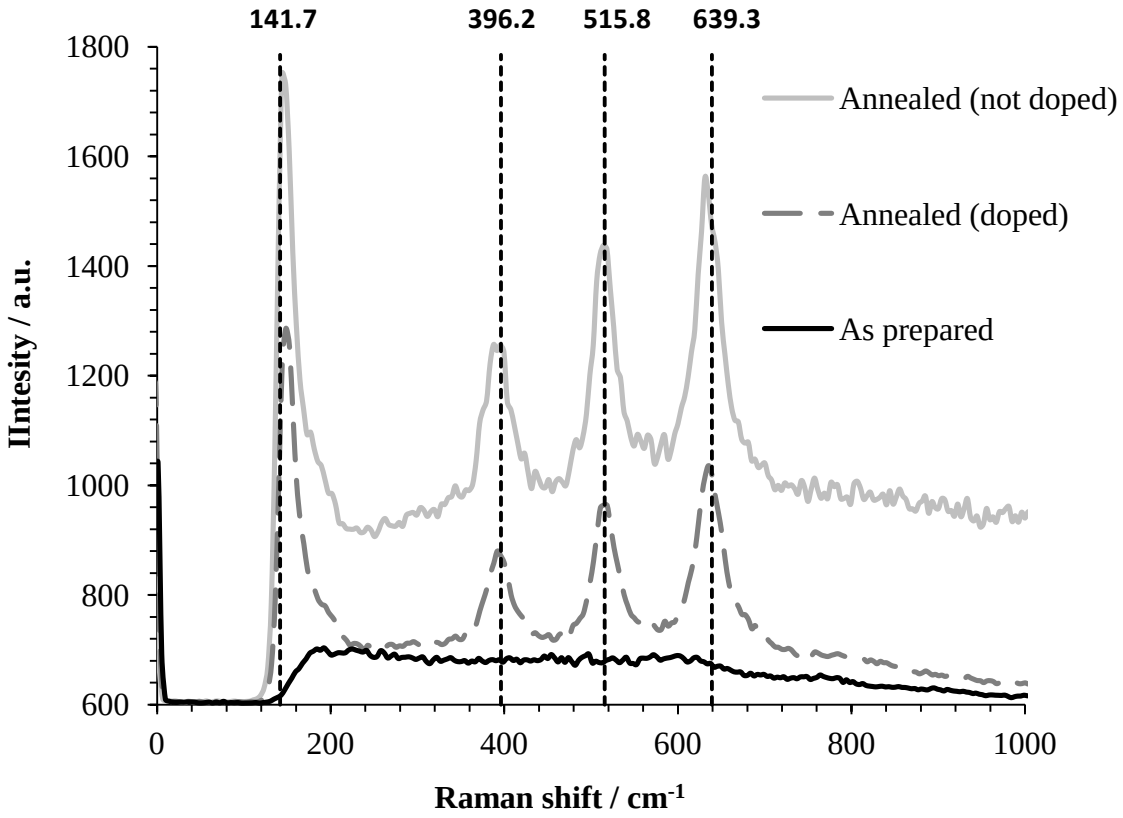
141.7
396.2
515.8
639.3
1800
1600
1400
1200
1000
800
600
IIntesity / a.u.
0
200
400
600
800
1000
Raman shift / cm-1
Annealed (not doped)
Annealed (doped)
As prepared

Figure 6

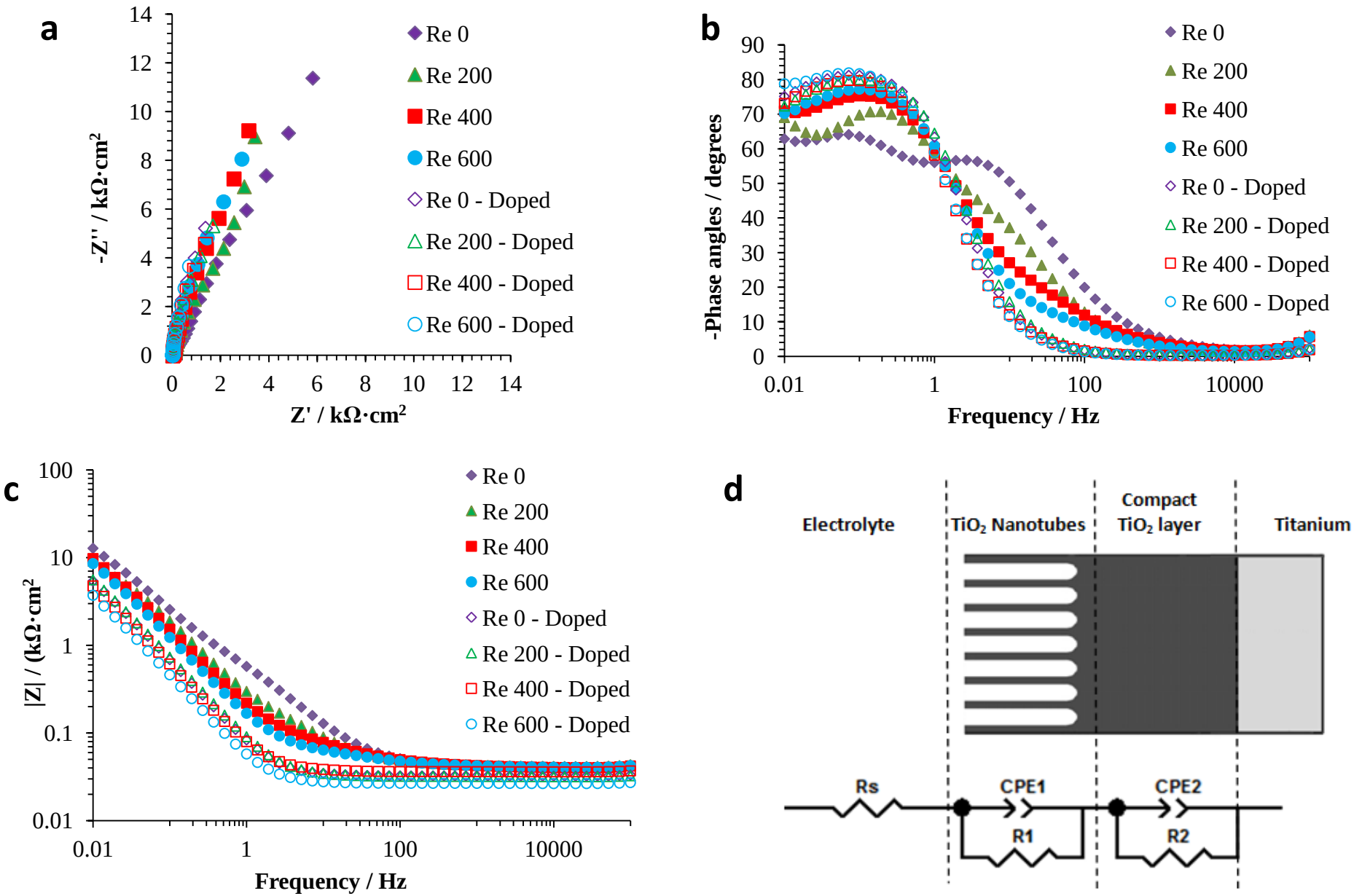
a
-Z'' / kΩ·cm²
Z' / kΩ·cm²
Re 0
Re 200
Re 400
Re 600
Re 0 - Doped
Re 200 - Doped
Re 400 - Doped
Re 600 - Doped
b
-Phase angles / degrees
Frequency / Hz
c
|Z| / (kΩ·cm²)
Frequency / Hz
d
Electrolyte
TiO2 Nanotubes
Compact TiO2 layer
Titanium
Rs
CPE1
CPE2
R1
R2

Figure 7

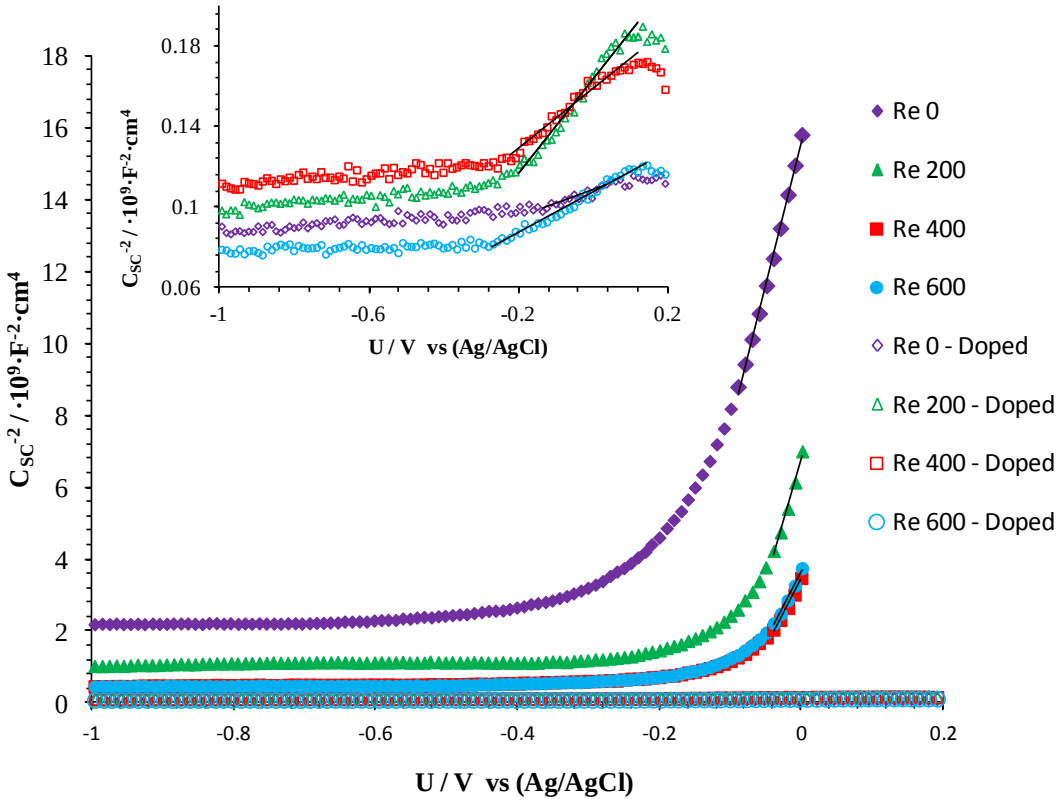
18
16
14
12
10
8
6
4
2
0
-1
-0.8
-0.6
-0.4
-0.2
0
0.2
C_{SC}^{-2} / ·10⁹·F⁻²·cm⁴
U / V vs (Ag/AgCl)
0.18
0.14
0.1
0.06
-1
-0.6
-0.2
0.2
C_{SC}^{-2} / ·10⁹·F⁻²·cm⁴
U / V vs (Ag/AgCl)
Re 0
Re 200
Re 400
Re 600
Re 0 - Doped
Re 200 - Doped
Re 400 - Doped
Re 600 - Doped

Figure 8

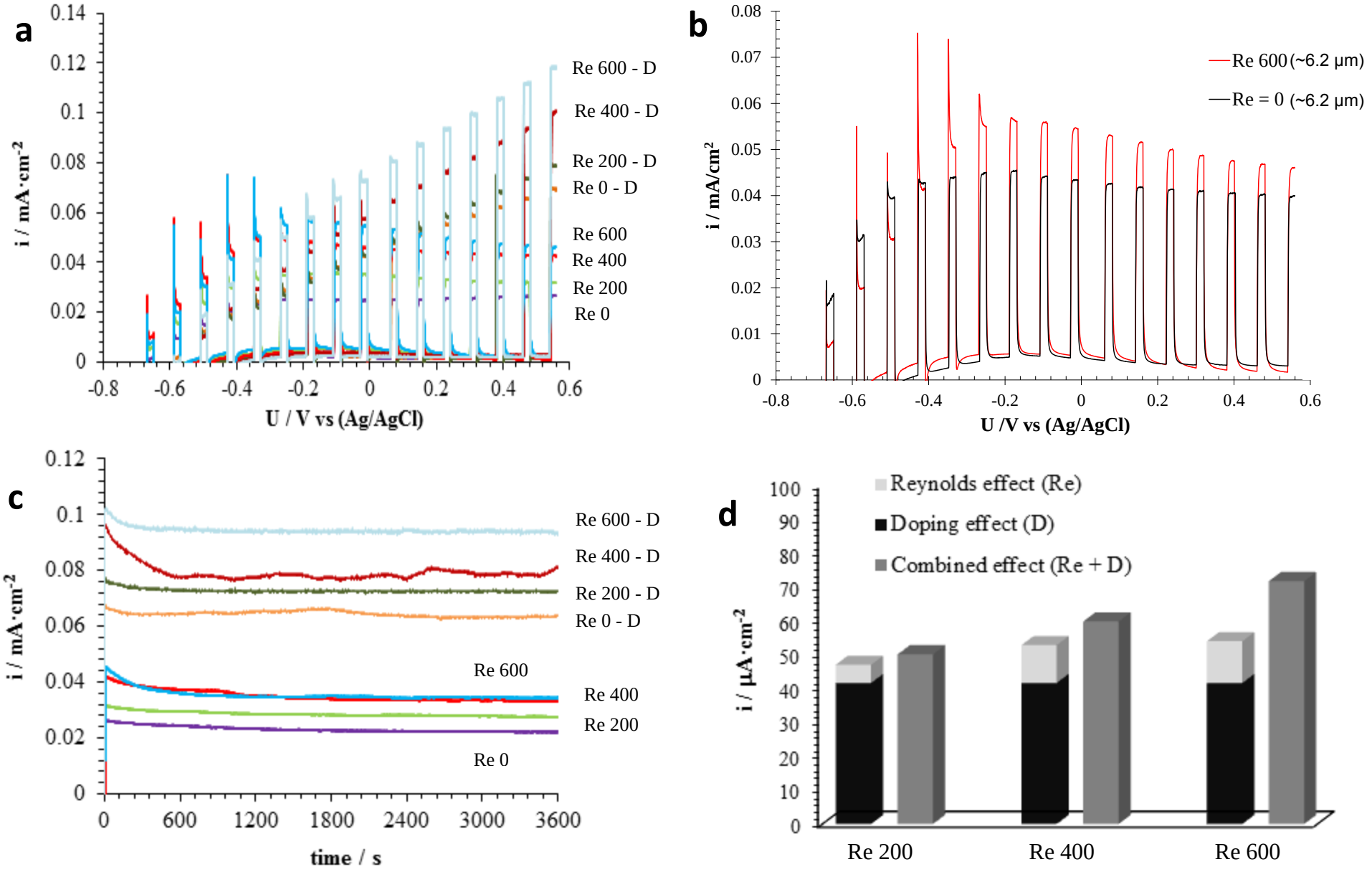
a
i / mA·cm-2
U / V vs (Ag/AgCl)
Re 600 - D
Re 400 - D
Re 200 - D
Re 0 - D
Re 600
Re 400
Re 200
Re 0
b
i / mA/cm2
U /V vs (Ag/AgCl)
Re 600 (~6.2 μm)
Re = 0 (~6.2 μm)
c
i / mA·cm-2
time / s
Re 600 - D
Re 400 - D
Re 200 - D
Re 0 - D
Re 600
Re 400
Re 200
Re 0
d
i / μA·cm-2
Reynolds effect (Re)
Doping effect (D)
Combined effect (Re + D)
Re 200
Re 400
Re 600